Supporting Information

Engineering Ru-N_4 single atom catalysts on Ni-MOF-derived porous graphitic carbon for pH universal water electrolysis

Biswajit Mishra, Swayamprakash Biswal, Bijay P. Tripathi*

Functional Materials and Membranes Laboratory, Department of Materials Science and Engineering, Indian Institute of Technology Delhi, Hauz Khas, New Delhi 110016, India

Email: bptripathi@mse.iitd.ac.in; drbptripathi@gmail.com

Table of Contents

S1. Materials and Methodologies

S1.1. Chemicals

Terephthalic acid, nickel nitrate hexahydrate and nafion solution (5 wt%) were procured from Alfa Aaser. Ruthenium (III) chloride hydrate, Potassium hydroxide, and Ruthenium oxide (RuO_2) were purchased from Sigma Aldrich, USA. Carbon fiber paper (Toray 060 - TGP-H-060, 5% wt-proofing, 190 µm thickness) was purchased from the Fuel cell store, USA. All chemicals are of analytical grade and were procured through commercial suppliers and utilized directly without additional purification steps. Unless otherwise mentioned, deionized water (DI) was used for all the synthesis and electrochemical analyses to minimize organic and trace-metal contamination.

S1.2. Synthesis of Ni-MOF

The pristine Ni-MOF was synthesized by employing terephthalic acid as the connecting organic linker and Nickel nitrate hexahydrate as the metallic node, following our previously reported methodology.[1] In a typical procedure, 1.5 mmol of terephthalic acid was first dissolved in 10 mL of dimethylformamide (Solution A), while an equimolar amount of Nickel nitrate hexahydrate salt was solubilized in 60 mL of deionized water (Solution B). Subsequently, the organic linker solution was added dropwise to Solution B at ambient conditions under vigorous stirring. Upon addition of the organic solution, the color of the reaction mixture changed to pale yellow. The resulting mixture was then transferred to a Teflon-lined autoclave and heated at 160 °C for 8 hours. After the completion of the reaction, the MOF was isolated via centrifugation and washed multiple times with DMF, water, and ethanol. Finally, the product was dried under vacuum, resulting in the formation of Ni-MOF.

S1.3. Synthesis of Ru_1/Ni-NPGC

Typically, 1 gm of Ni-MOF was dispersed in 50 mL of deionized water and sonicated to achieve a homogeneous dispersion. Subsequently, 1.5 grams of semicarbazide were added to

the MOF dispersion and stirred continuously for 2 hr. Then, a Ruthenium chloride solution (2 wt% of Ni-MOF) was added dropwise to the mixture and stirred continuously for 6 hr at room temperature. The resulting mixture was frozen and dried using a freeze dryer. The obtained powder was transferred to a crucible with a lid and pyrolyzed at 600 °C with a heating rate of 2 °C/min under Argon flow. Afterward, the product was collected and washed several times with deionized water, followed by drying under vacuum at 60 °C. Unless otherwise mentioned, the product was referred to as Ru_1/Ni-NPGC throughout the manuscript. For comparison, the pristine Ni-MOF was pyrolyzed under similar conditions without the Ru precursor salt, yielding Ni nanoparticles supported on porous graphitic carbon, referred to as Ni-NPGC. A similar procedure was followed to produce samples with different Ru loadings by using 1, 3, 4, and 5 wt% of $RuCl_3$ precursor salt.

S1.4. Instrumentation

Powder X-ray powder diffraction pattern was collected on an Empyrean (Malvern PANalytical) diffractometer to characterize the crystallinity of the samples. To determine the surface area and porosity of synthesized electrocatalyst, N_2 adsorption/desorption isotherm was collected on a Autosorb-iQ XR analyzer, Quantachrome Instruments. Prior to analysis, the samples were degassed at 150 °C for 16 hr and the ASiQwin software was used to obtain the information about surface area, pore size and distribution etc. The surface elemental composition and state of the catalyst was evaluated using X-ray photoelectron spectroscopy (AXIS Supra spectrometer, Kratos Analytical Ltd). In situ Raman and FTIR analysis were conducted using our customized electrochemical set up and the potential was provided during the electrolysis using a CHI instruments.[1, 2] Aberration correction High-angle annular dark-field scanning transmission electron microscopy (HAADF-STEM) images were recorded using FEI TITAN microscope. STEM elemental mapping images were collected using TESCAN MAGNA (TESCAN instruments) operating at 30 kV accelerating voltage. Field-emission

scanning electron microscopy (FESEM) images were conducted using a JSM-7800F Prime, JEOL instruments. Before analysis, the samples were dispersed and mounted over a microscopic glass slide and coated with a thin Pt layer using a sputter coater. High-resolution transmission electron microscopy (HRTEM) images were recorded using a JEM-ARM200F NEOARM (JEOL, Japan) at an accelerating voltage of 200 kV. Raman spectra were collected on a Micro Raman spectrometer (Renishaw plc, UK). equipped with an Ar laser source. Inductively Coupled Plasma Mass Spectrometry (ICP-MS) was used to determine the metal content of different electrocatalyst. X-ray absorption spectroscopy (XAS) analysis of Ru K-edge spectra for Ru_1/Ni-NPGC, $RuCl_3$, Ru-foil, and RuO_2 were collected at Indus-2 beamline of the RRCAT synchrotron radiation facility (Applied spectroscopy division, BARC, India). The standard XAS data for Ru-foil and RuO_2, previously used in our earlier publication, were included in this study as well.[1] XANES spectra underwent various procedures, such as background subtraction, calibration, and normalization, to obtain experimental absorption coefficients plotted against energies (μ(E)). EXAFS data were simulated using the ATHENA module and FEFF software package, with Ru-foil and RuO_2 as reference materials for analysis.

S1.5. Electrochemical measurements

The electrochemical measurements were conducted using a conventional three-electrode cell set-up equipped with an Autolab M204 (*Serial No. MAC90559, Metrohm*) workstation. In this three-electrode set up, Pt foil (1 cm^2) working as counter electrode, Ag/AgCl as reference electrode and catalyst was mounted over a glassy carbon electrode serves as working electrode. To prepare working electrode, ~4 mg of catalysts was dispersed in a 0.8 ml of DI water and ethanol (3:1) along with 30 μL of 5 wt% Nafion solution through ultrasonication. The resulting ink was pipetted (~5 μL) and dropped onto a 3 mm diameter glassy carbon electrode (0.07 cm^2 area) and dried at room temperature. The active mass loading of electrocatalyst is calculated to be ~0.35 mg cm^{-2}. For both HER and OER, the linear sweep voltammetry (LSV) curve was

obtained with a rotation speed of 1600 r.p.m. at a scan rate of 1 mV sec^{-1}. The LSV spectra were iR compensated to 90% to avoid resonance and reduce experimental errors. All potentials were converted to a reversible hydrogen electrode (RHE) using this equation (E (V vs RHE) = E (V vs Ag/AgCl) + 0.194 V + 0.0591 pH). The overpotential (η) was estimated by η = E(vs. RHE) V for HER and η = E(vs. RHE) –1.23 V for OER, respectively. To calculate the activation energy (E_a) of the electrocatalyst, LSV was performed at different temperatures, and the activation energy was calculated using the Arrhenius equation. Electrochemical impedance spectroscopy (EIS) spectra were obtained across frequencies ranging from 0.1–100 kHz., with an applied voltage amplitude of 5 mV. The stability of electrocatalyst were assessed by long-term chronoamperometry measurements. Cyclic voltammetry curves were acquired at various scan rates (10-50 mV s^{-1}) within the non-faradaic region to estimate the electrochemical double layer capacitance (C_{dl}). Subsequently, the C_{dl} value was divided by the specific capacitance to determine the electrochemical active surface area (ECSA). The Faradaic efficiency and Turn over frequency was estimated using our previously reported literature.[3]

S1.5.1. Electrochemical active surface area (ECSA) calculation

The electrochemical surface area (ECSA) of the electrocatalyst is directly proportional to its electrochemical double-layer capacitance (C_{dl}). To determine C_{dl}, cyclic voltammetry (CV) measurements are performed at different scan rates within the non-faradaic current region. Accordingly, potential sweeps ranging from 0.82 V to 0.92 V vs. RHE were conducted at scan rates varying from 10 to 50 mV s^{-1}. The relationship between the double-layer charging current (ic) and the scan rate is expressed as:

$$i_c = \nu c_{dl}$$

The slope of the plot of charging current against scan rate corresponds to the double-layer capacitance (C_{dl}). The ECSA is then calculated using the following equation.[4]

$$ECSA = \frac{C_{dl}}{C_s} S$$

The specific capacitance in 1 M NaOH typically ranges from 0.035 to 0.06 mF/cm². For the ECSA calculation in this study, the upper limit value of Cs was set to 0.04 mF/cm².[3, 5] Here, "S" represents the actual surface area of a smooth metal electrode, which is typically equivalent to the geometric area of the glassy carbon electrode (S=0.196 cm^2)

S1.5.2. Turn over frequency (TOF) and number of active sites per electrode area calculation

TOF values of electrocatalysts were calculated using the following equation given below, [6]

$$TOF = \frac{\text{Total number of } O_2 \text{ turnover per geometric area } (cm^2)}{\text{Total no of active sites per geometric area } (cm^2)}$$

The total amount of O_2 produced per unit area was calculated using the current density (j) obtained from the LSV polarization curve equations.

$$= \left(|J|\ \frac{mA}{cm^2}\right)\left(\frac{C/_S}{1000\ mA}\right)\left(\frac{1\ mol}{96453.8\ C}\right)\left(\frac{6.023\times10^{23}}{1 mol O_2}\right)$$

$$= 1.56 \times\ 10^{15}\ \frac{O_2/s}{cm^2} per\ \frac{mA}{cm^2}$$

Based on the assumption that each ruthenium atom in the catalyst acts as an active site, supported by findings from electrocatalytic and in situ experiments, the number of ruthenium atoms was calculated using its molar mass and the catalyst's mass deposited on the glassy carbon electrode. ICP-MS analysis determined the ruthenium content to be 1.75 %, with the catalyst loading on the electrode surface estimated at around 0.35 mg cm^{-2}.

The number of active sites per geometric area can be determined using following equation,[6]

$$\frac{0.35\ mg/cm^2 \times 10^{-3} \times 1.75\% \times 6.023 \times 10^{23}}{101.7\ g/mol}$$

$=3.62 \times 10^{16}$ active sites/cm^2

The TOF of Ru_1/Ni-NPGC was determined using the current density derived from the LSV polarization curves, applying the following equation:

$$TOF = \frac{1.56 \times 10^{15}}{5.96 \times 10^{16}} |J| = 0.0261\ |J|$$

S1.6. Electrochemical measurements for overall water splitting

The complete electrolyzer setup was assembled within a two-electrode cell, where the Ru_1/Ni-NPGC was positioned on a Toray carbon paper, functioning as both the cathode and anode (Ru_1/Ni-NPGC || Ru_1/Ni-NPGC). A similar approach was utilized to prepare the catalyst ink, which was then applied onto carbon paper and left to dry at room temperature.

S2. Characterization of pristine Ni-MOF

S2.1. Powder X-ray diffraction analysis

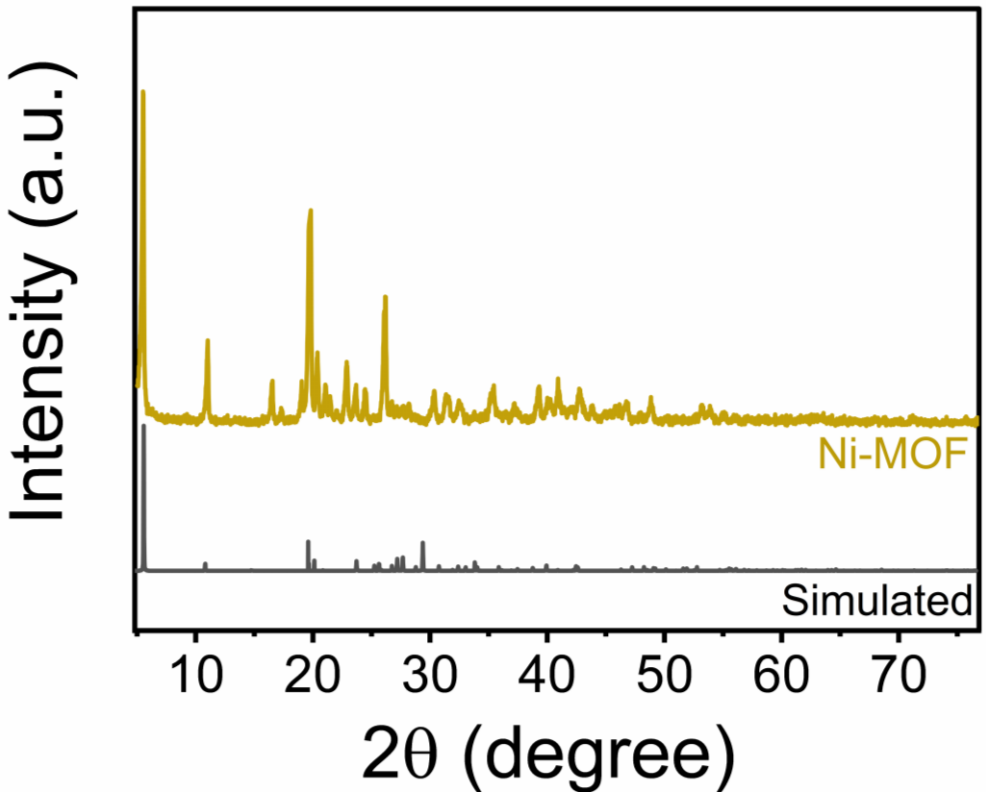

Figure S1: PXRD spectra of pristine Ni-MOF

S2.2. FESEM-EDX and TEM of neat MOF

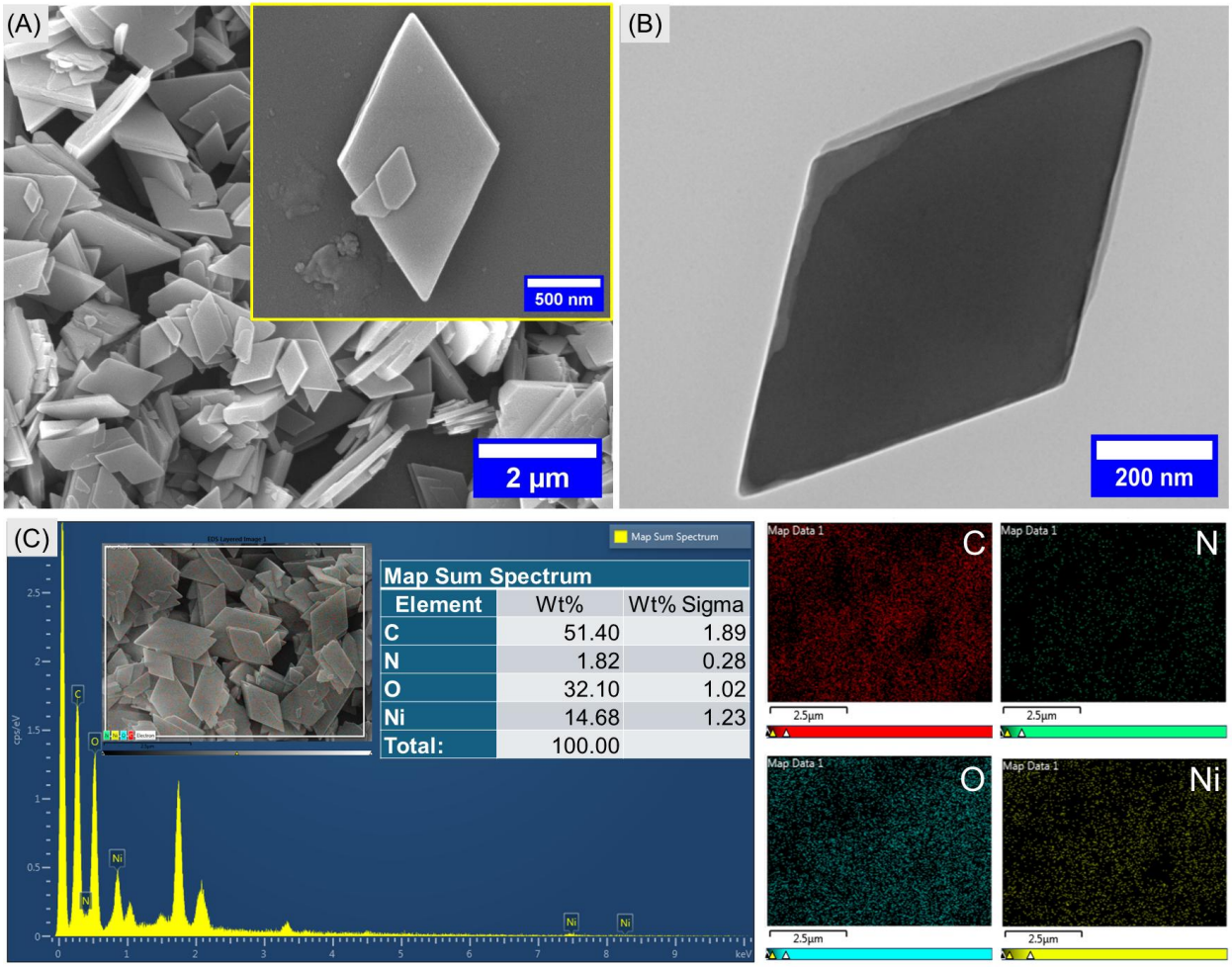

Figure S2: Electron microscopic analysis of pristine Ni-MOF. (A) FESEM, (B) TEM image of Ni-MOF, (C) FESEM-EDS mapping images of Ni-MOF.

S2.3. Stability of Ni-MOF in acidic solution

The stability of Ni-MOF was examined by subjecting it to acidic environment (100 mM HCl) at 50 °C for 48 hours. As presented in **Figure S3 (Supp. Info.),** Ni-MOF preserved its crystalline structure despite extended exposure to acidic conditions. Moreover, FESEM analysis revealed that the framework retained its integrity and demonstrated excellent stability.

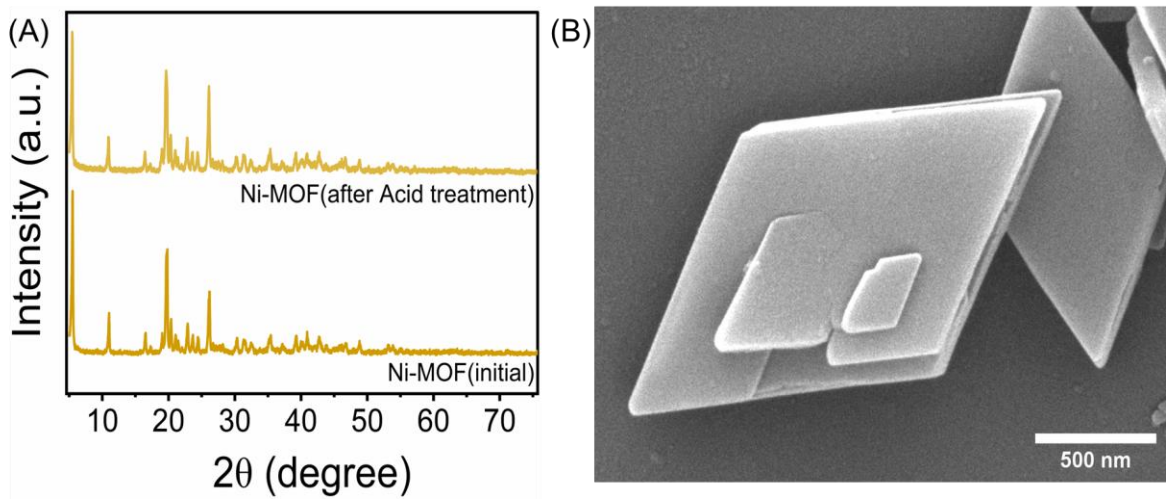

Figure S3: Stability test of pristine Ni-MOF in acidic solution. (A) PXRD spectra before and after exposure to acidic solution, (B) FESEM image after the stability test

S3. Characterization of electrocatalyst (Ru_1/Ni-NPGC)

S3.1 Effect of $RuCl_3$ concentration

We varied the concentration of $RuCl_3$ while maintaining consistent pyrolysis conditions to verify the formation of Ru nanoparticles at different salt concentrations. Initially, we performed PXRD analysis; however, we did not observe significant diffraction peaks corresponding to Ru nanoparticles **(Figure S4A).** Therefore, we conducted TEM (HR-TEM) analysis to verify the formation of Ru nanoparticles at higher $RuCl_3 \cdot H_2O$ concentrations. At 2 wt% $RuCl_3$ concentration (actual loading 1.75 wt%, determined via ICP-MS), we did not observe the formation of Ru nanoparticles. However, when the concentration was increased to 3 wt%, TEM analysis revealed the presence of small-sized Ru nanoparticles **(Figure S4B).** HRTEM analysis showed large-sized nanoparticles, which can be attributed to the presence of Ni nanoparticles. Additionally, small-sized particles were also observed in the HRTEM images. To confirm this, we analyzed the interplanar spacing of the two differently sized particles. The larger nanoparticles (~8 nm in size) exhibited an interplanar spacing of 0.200 nm, corresponding to the Ni (111) plane of nickel nanoparticles.[7] The smaller nanoparticles (~3 nm in size)

demonstrated an interplanar spacing of 0.209 nm, which can be attributed to the Ru (101) plane of Ru nanoparticles.[8] These findings confirm that the optimal loading for the formation of Ru SAC is 2 wt% $RuCl_3$. Beyond this concentration, Ru nanoparticle formation begins. To evaluate the electrocatalytic OER activity, we varied the $RuCl_3$ concentration **(Figure S18).** Our results indicate that increasing the $RuCl_3$ concentration leads to a decline in electrocatalytic OER activity, with the best performance observed at a Ru loading of 2 wt%. This suggests that the formation of Ru nanoparticles at higher $RuCl_3$ salt concentrations deteriorates the electrocatalytic activity, while the presence of Ru SAC sites enhances the electrochemical reaction.

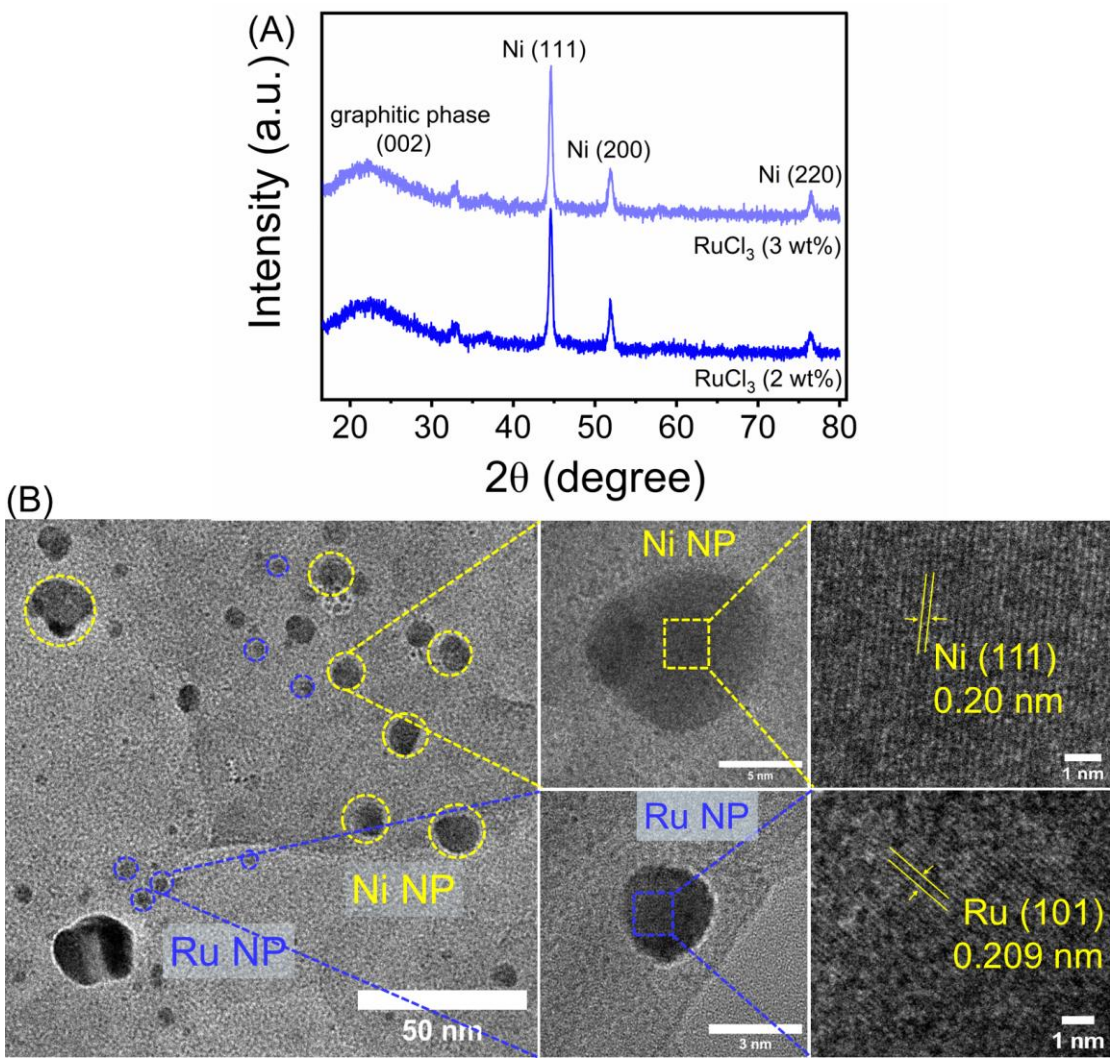

Figure S4: (A) PXRD spectra of different $RuCl_3$ loading sample, (B) HRTEM images of RuNP/Ni-NPGC (3 wt%)**.** (NP refers to Nanoparticle in the Figure)

S3.2. Raman spectra of Ru_1/Ni-NPGC

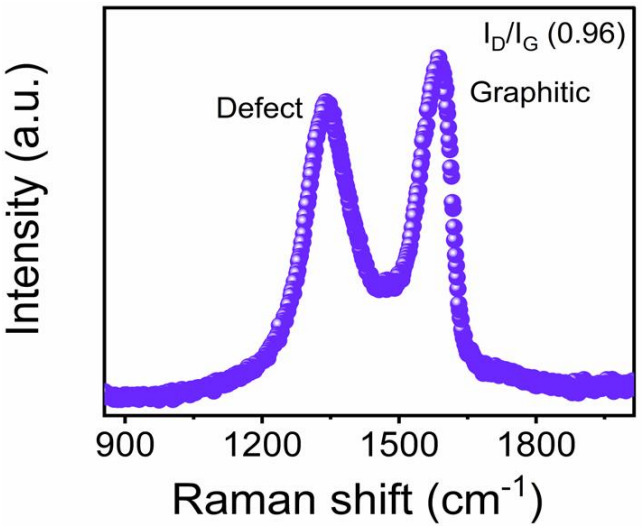

Figure S5: Raman spectra of Ru_1/Ni-NPGC

S3.3. BET surface area and pore-size analysis

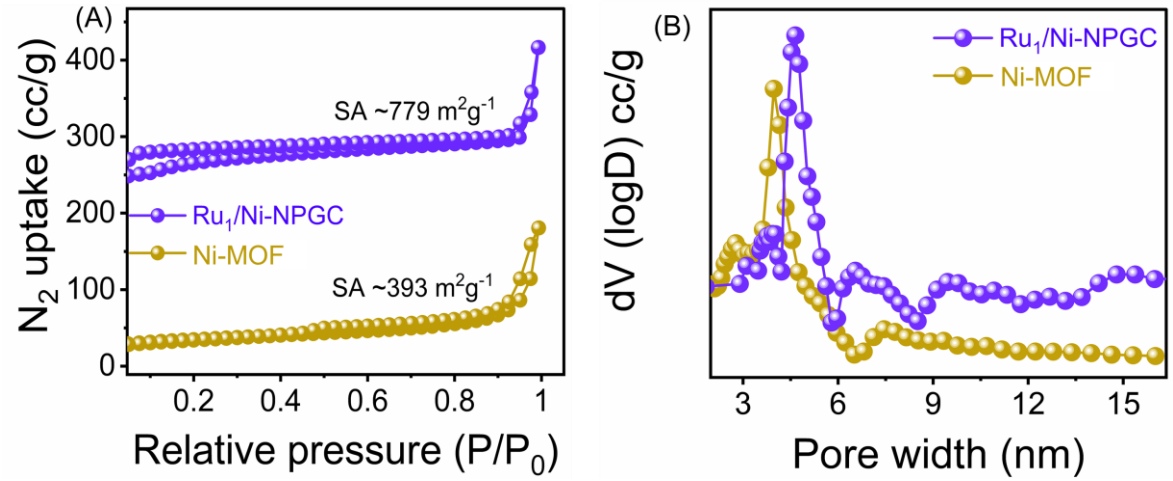

Figure S6: (A) N_2 adsorption/desorption isotherms, (B) Pore-size analysis estimated using non-local density functional theory (NLDFT) calculations.

S3.4. FESEM-EDX and HRTEM images of Ru_1/Ni-NPGC

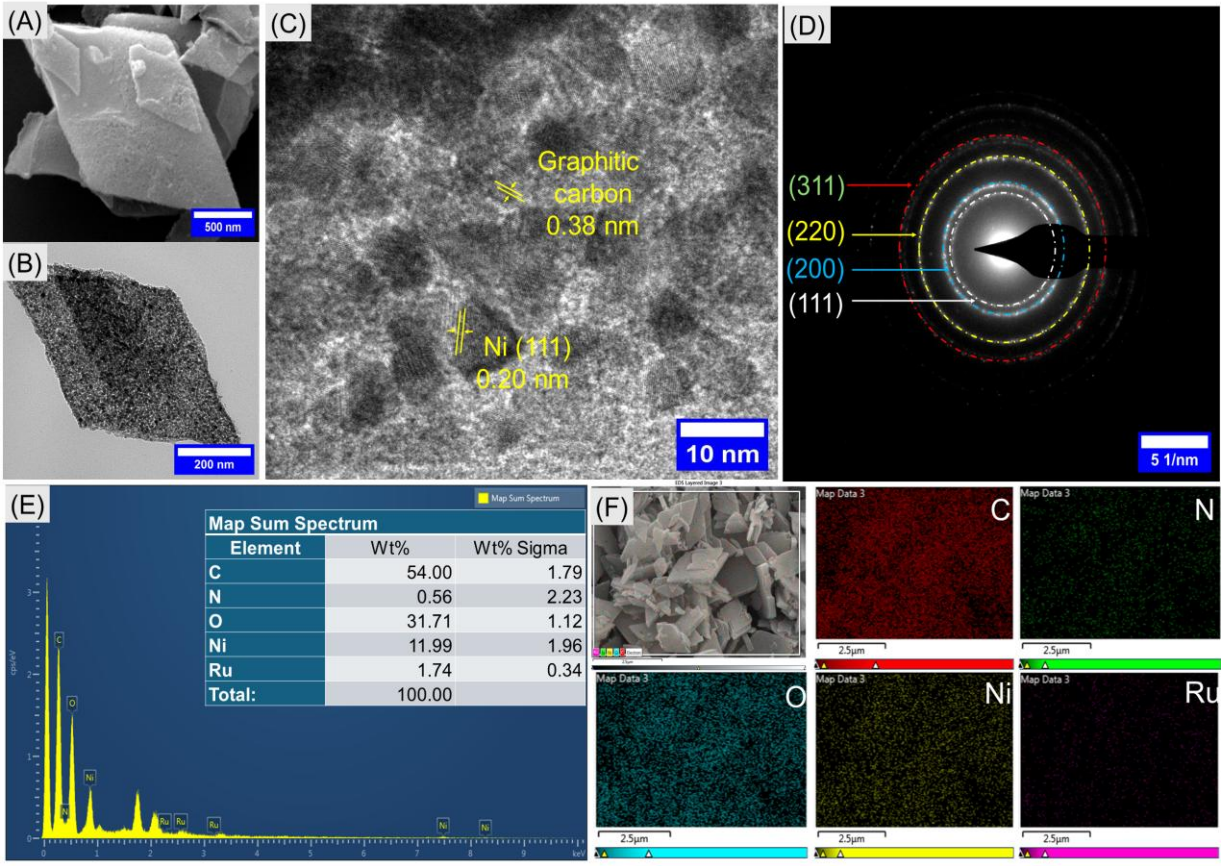

Figure S7: Electron microscopic analysis of synthesized electrocatalyst. (A) FESEM, (B) TEM image of Ru_1/Ni-NPGC, (C) High-resolution TEM image of Ru_1/Ni-NPGC, (D) selected area electron diffraction (SAED) pattern of Ru_1/Ni-NPGC, (E, F) FESEM-EDS-Mapping images of Ru_1/Ni-NPGC.

S3.5. X-ray photoelectron spectroscopy analysis

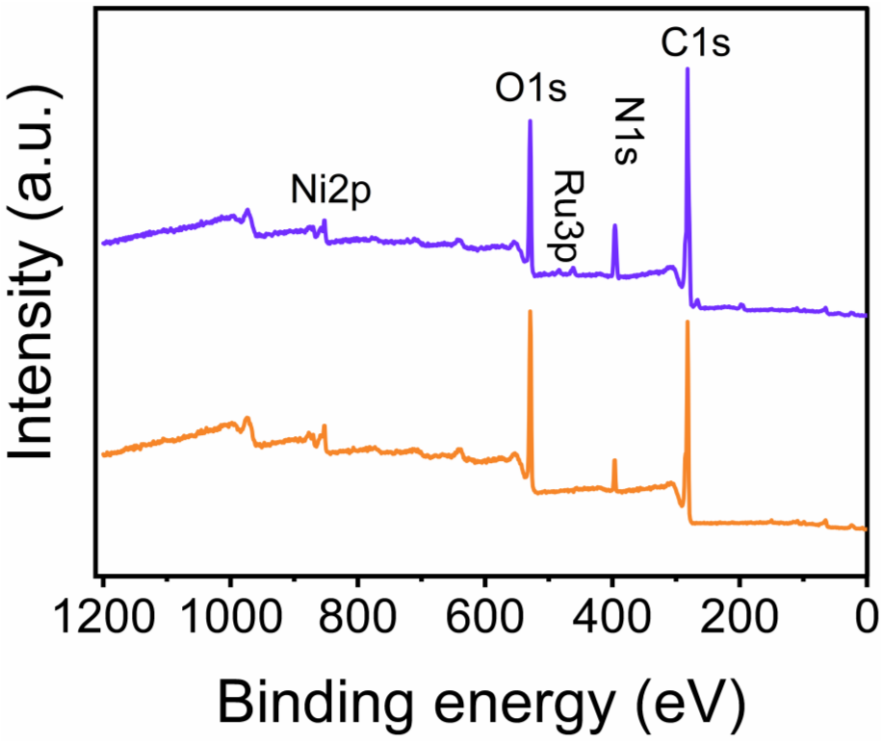

Figure S8: XPS survey spectra of pristine Ni-MOF and Ru_1/Ni-NPGC

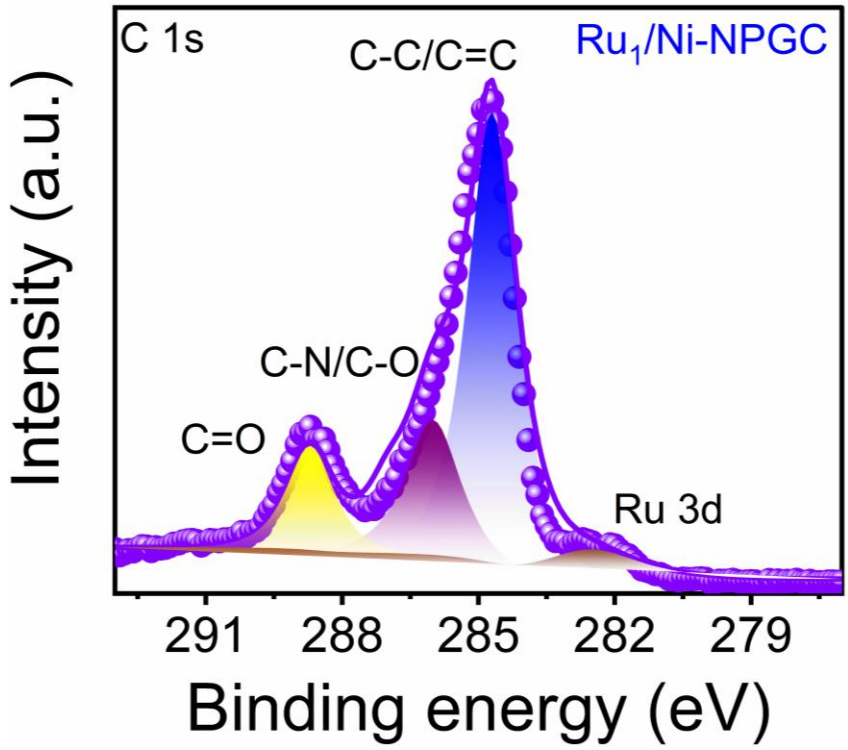

Figure S9: Deconvoluted C1s spectra of Ru_1/Ni-NPGC

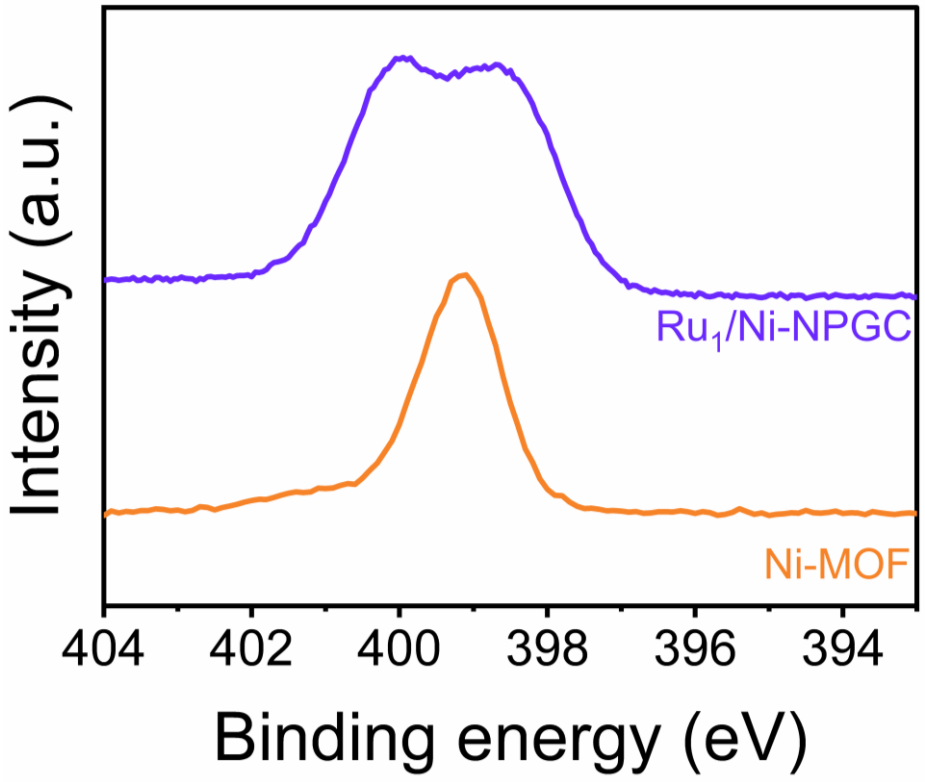

Figure S10: Comparative N1s spectra of Ni-MOF and Ru_1/Ni-NPGC

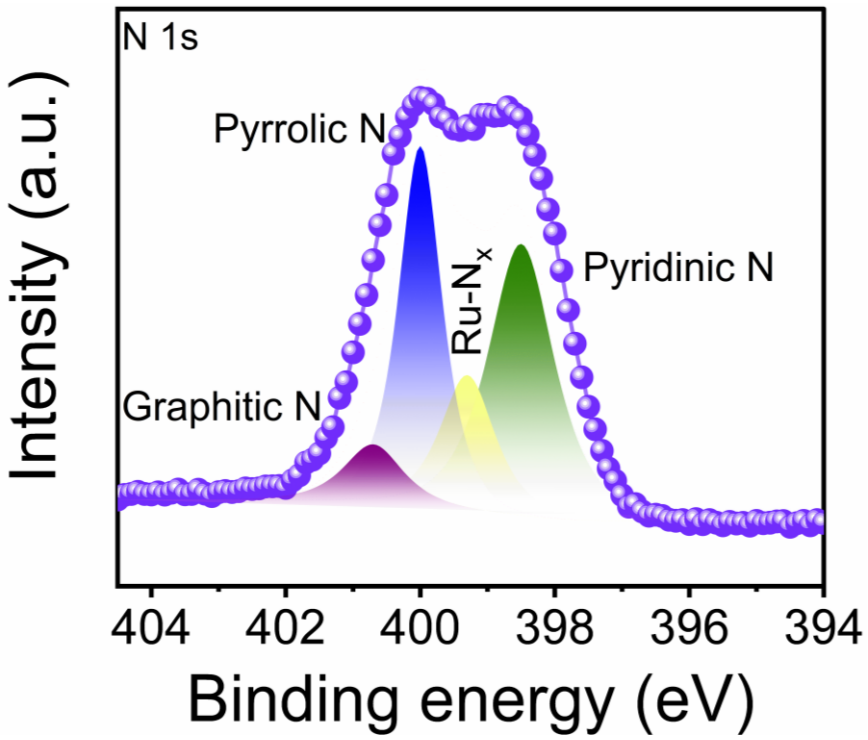

Figure S11: Deconvoluted N1s spectra of Ru_1/Ni-NPGC

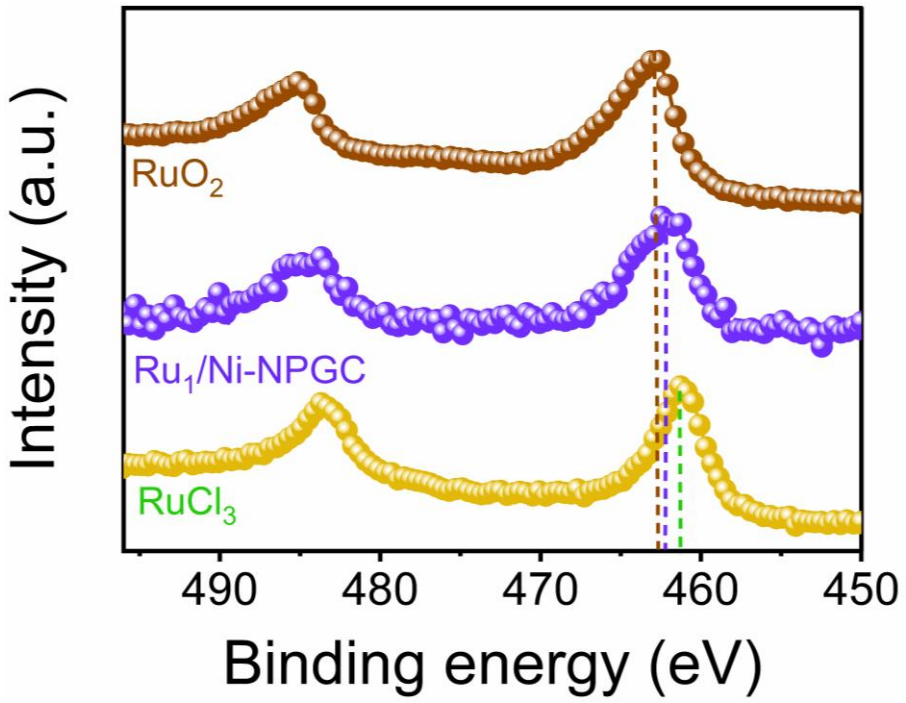

Figure S12: Comparative Ru 3p spectra of Ru_1/Ni-NPGC with RuO_2 and $RuCl_3$

S3.6. X-ray absorption spectroscopy analysis

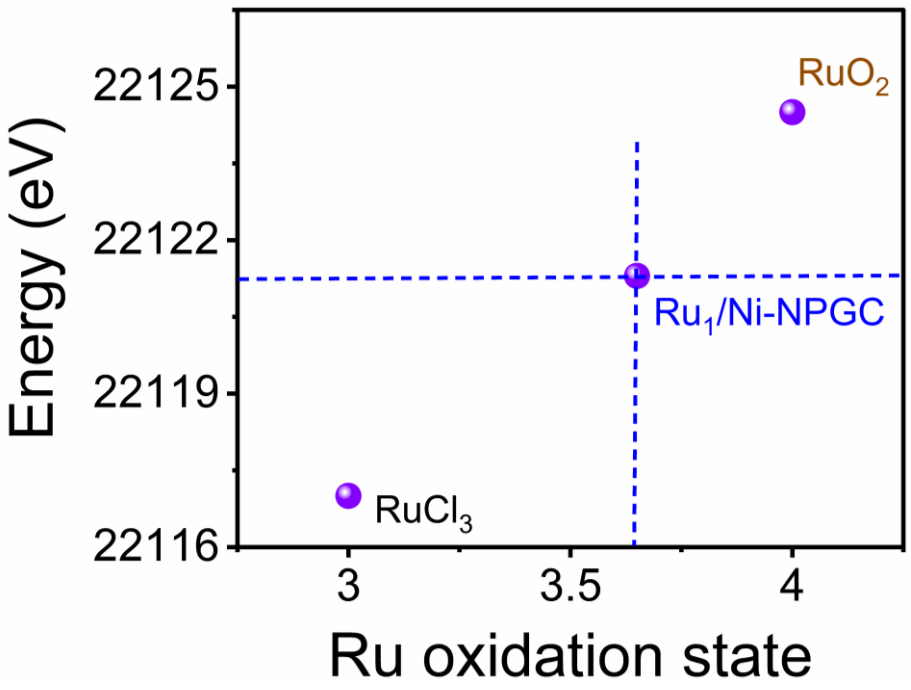

Figure S13: Oxidation state of Ru_1/Ni-NPGC determination using XAS analysis

S3.7. Fitting of EXAFS spectra

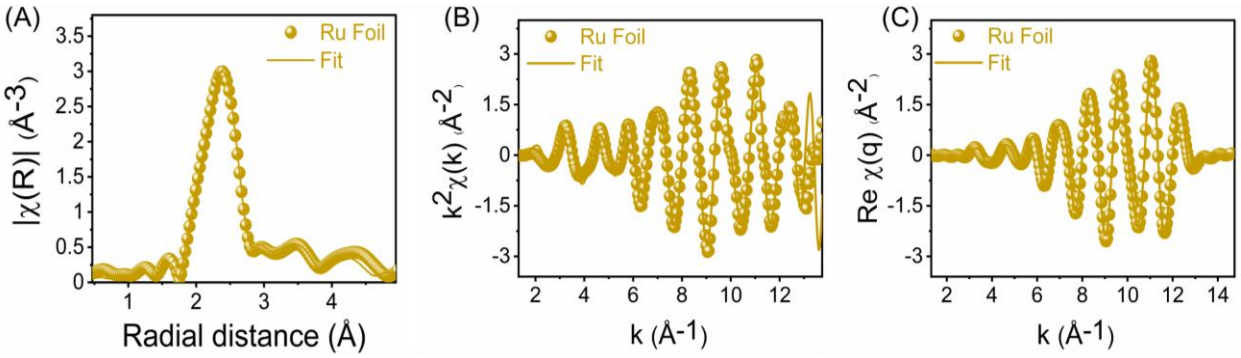

Figure S14: (A) R-space, (B) k, (C) q-space fitting plot of Ru foil

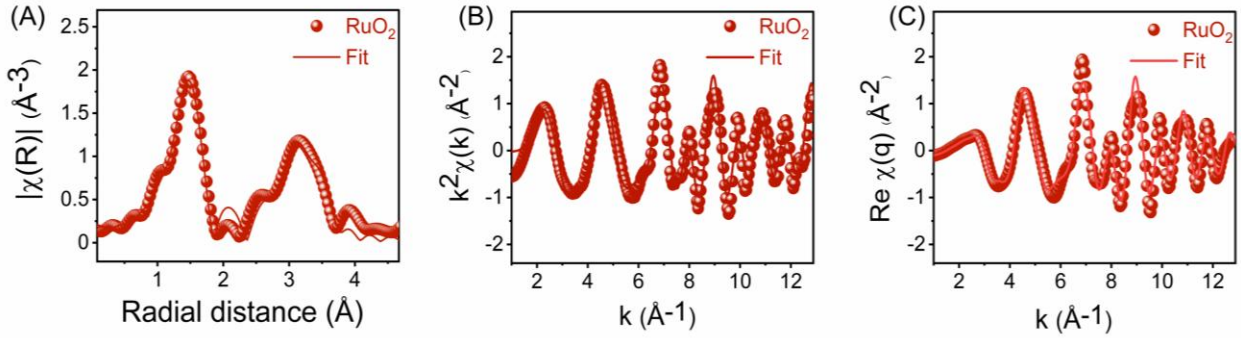

Figure S15: (A) R-space, (B) k, (C) q-space fitting plot of RuO_2

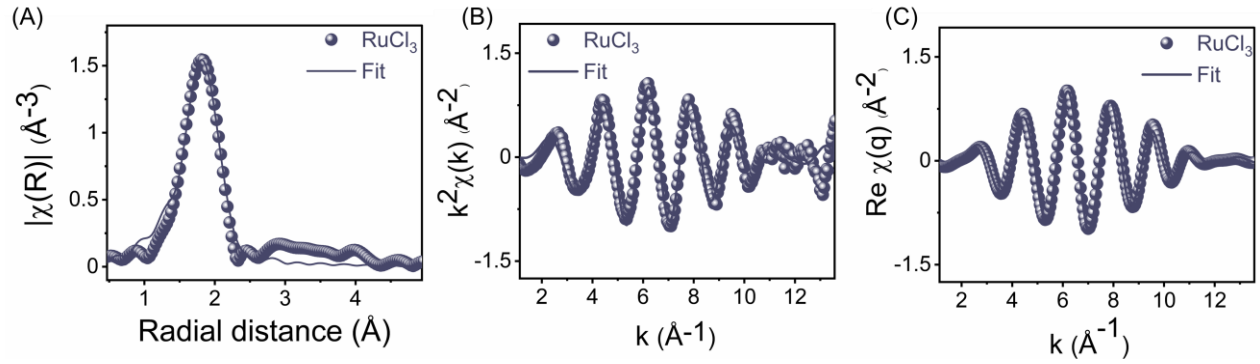

Figure S16: (A) R-space, (B) k, (C) q-space fitting plot of $RuCl_3$

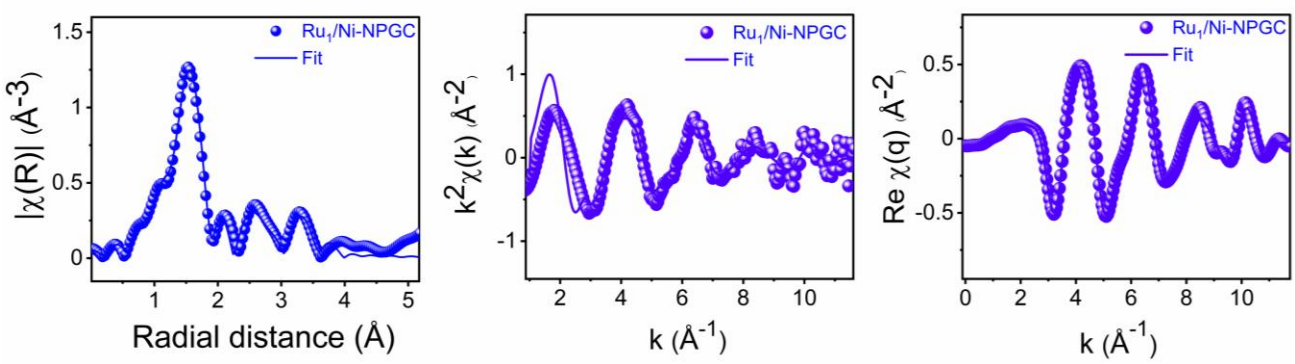

Figure S17: (A) R-space, (B) k, (C) q-space fitting plot of Ru_1/Ni-NPGC

S4. Additional data for the electrocatalytic OER activity

S4.1. Working electrode preparation and Electrochemical measurement setup

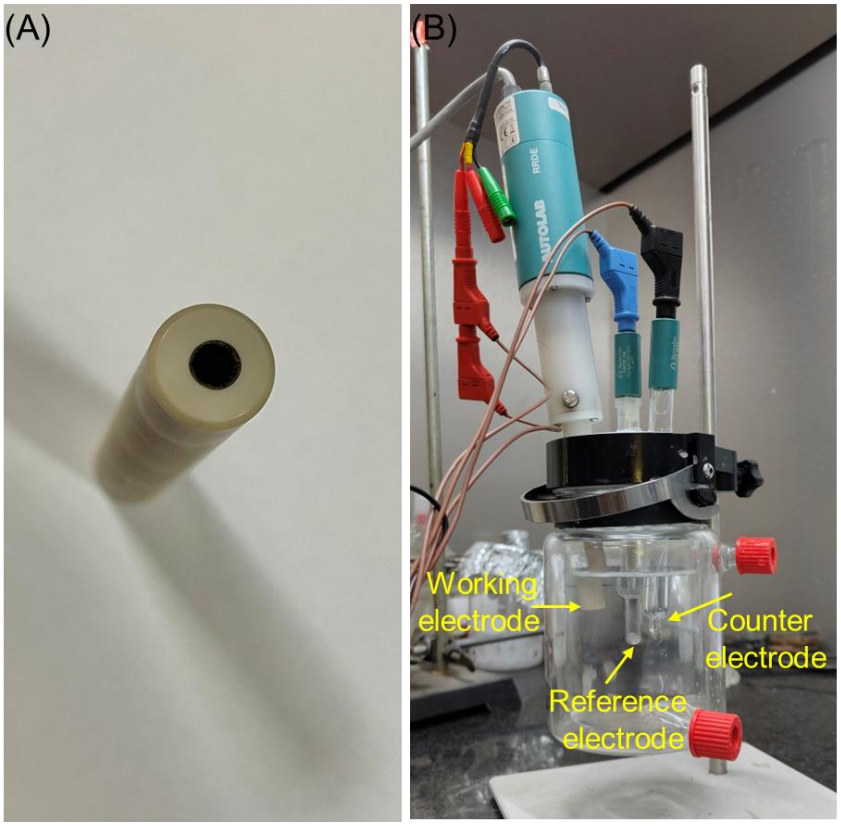

Image S1: (A) Electrocatalyst mounted on a glassy carbon electrode (3 mm diameter), (B) conventional Three electrode cell setup.

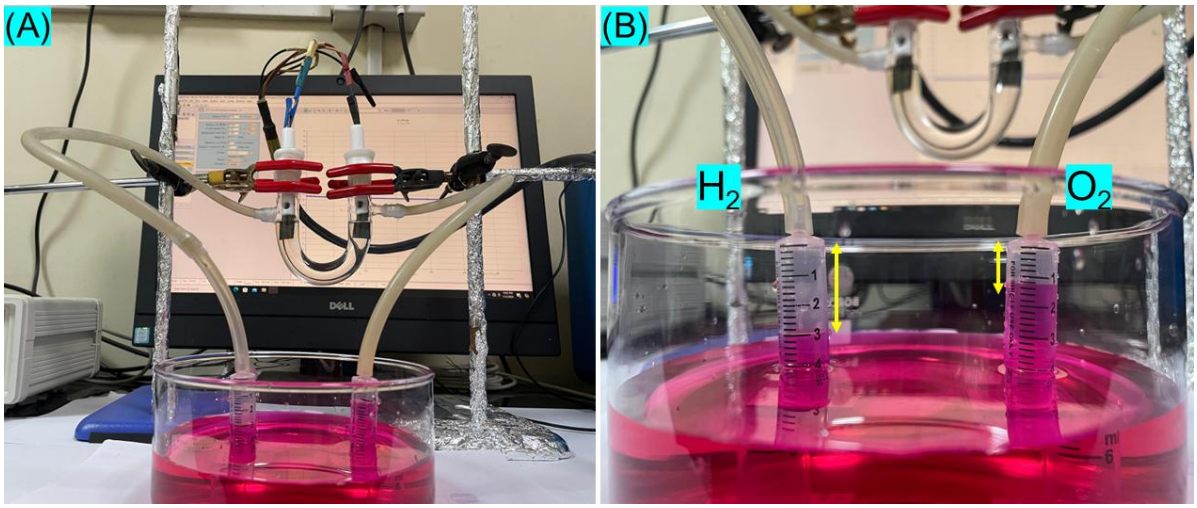

Image S2: (A, B) Lab equipment to measure the H_2 and O_2 production rates.

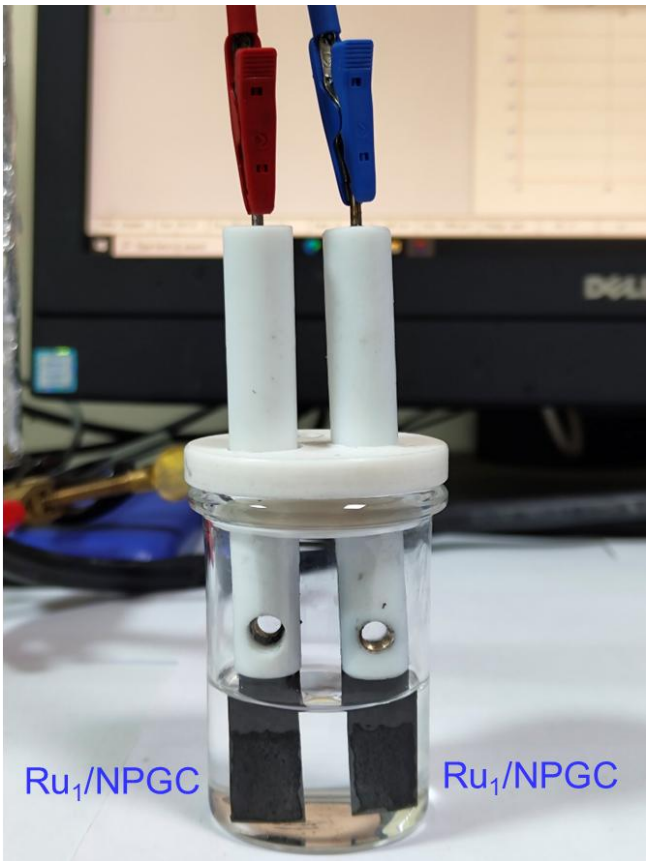

Image S3: Two electrode set up for the overall water splitting

S4.2. Effect of Ru loading on electrocatalytic activity

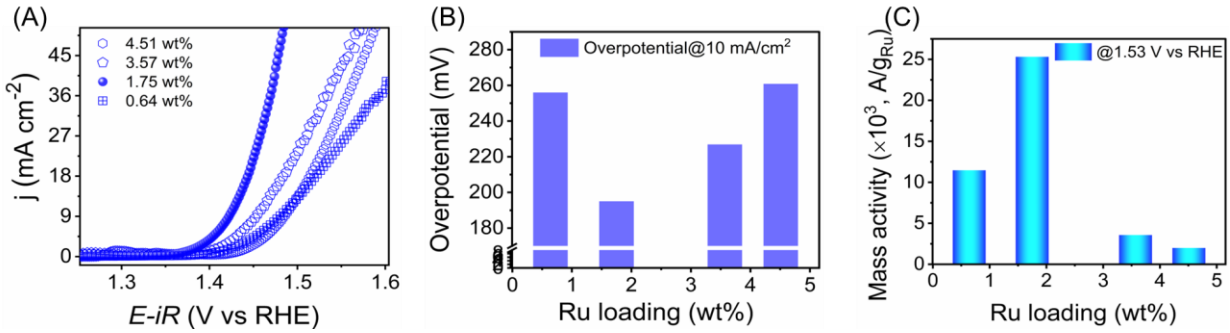

Figure S18: Effect of Ru loading on Ni-MOF on electrocatalytic OER activity, (A) LSV spectra, (B) Corresponding overpotential at 10 mA/cm^2, (C) Mass activity**.**

S4.2. LSV spectra of pristine Ni-MOF and Ni-NPGC

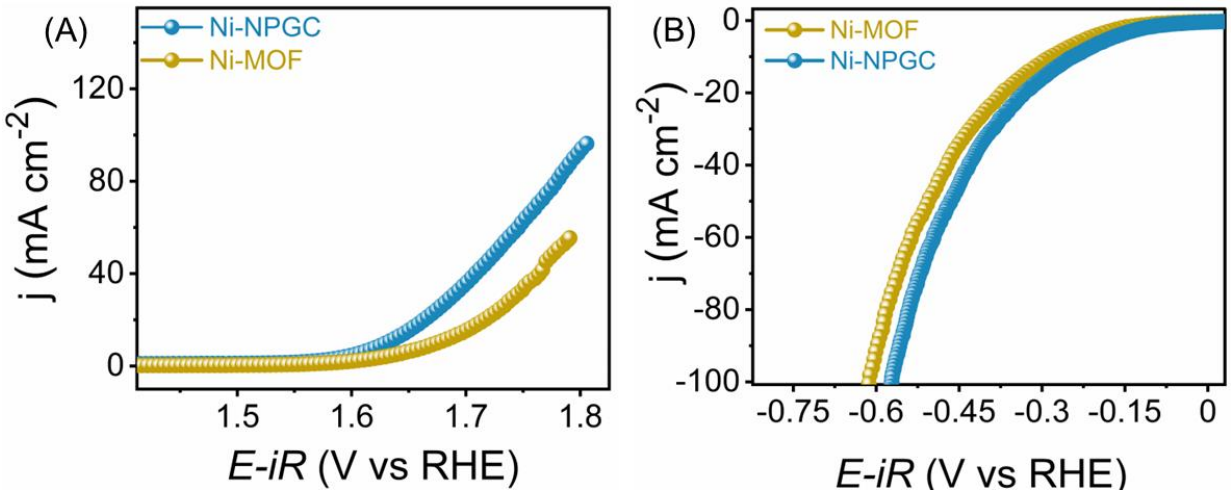

Figure S19: (A) OER and (B) HER LSV polarization curves for Ni-MOF and Ni-NPGC in O_2-saturated 1 M KOH solution.

S4.3. iR compensated LSV spectra

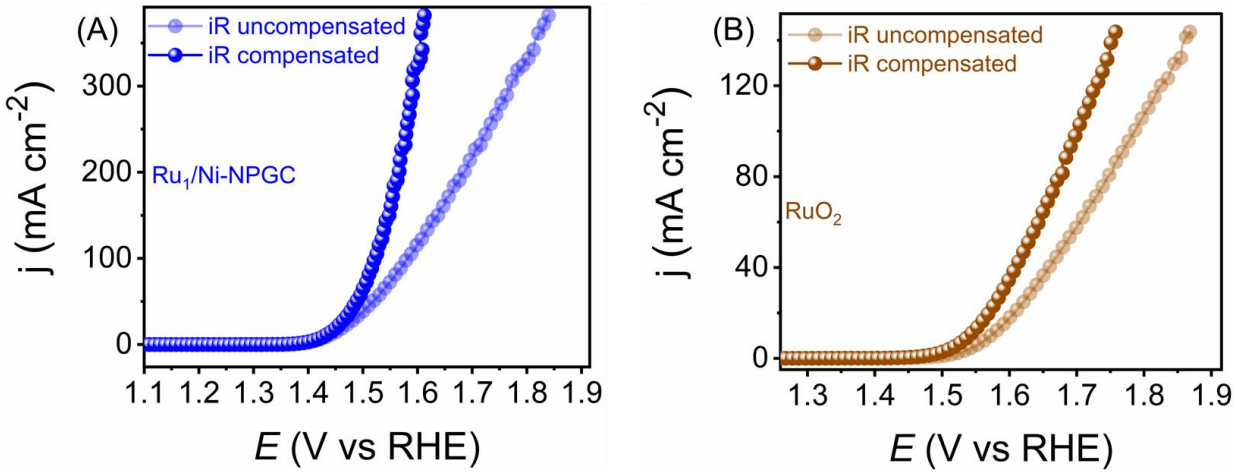

Figure S20: OER LSV polarization curves in O2-saturated 1 M KOH solution, 90% iR-compensated (A) Ru_1/Ni-NPGC, (B) RuO_2.

S4.4. Overpotential at different current density

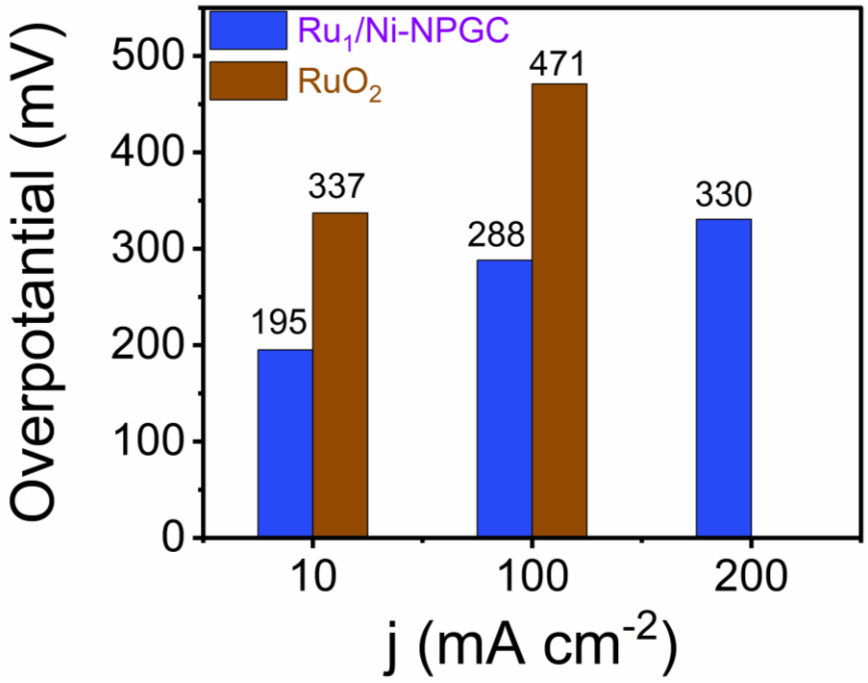

Figure S21: Overpotential required by RuO_2 and Ru_1/Ni-NPGC for OER

S4.5. LSV curve after long-term CV cycles

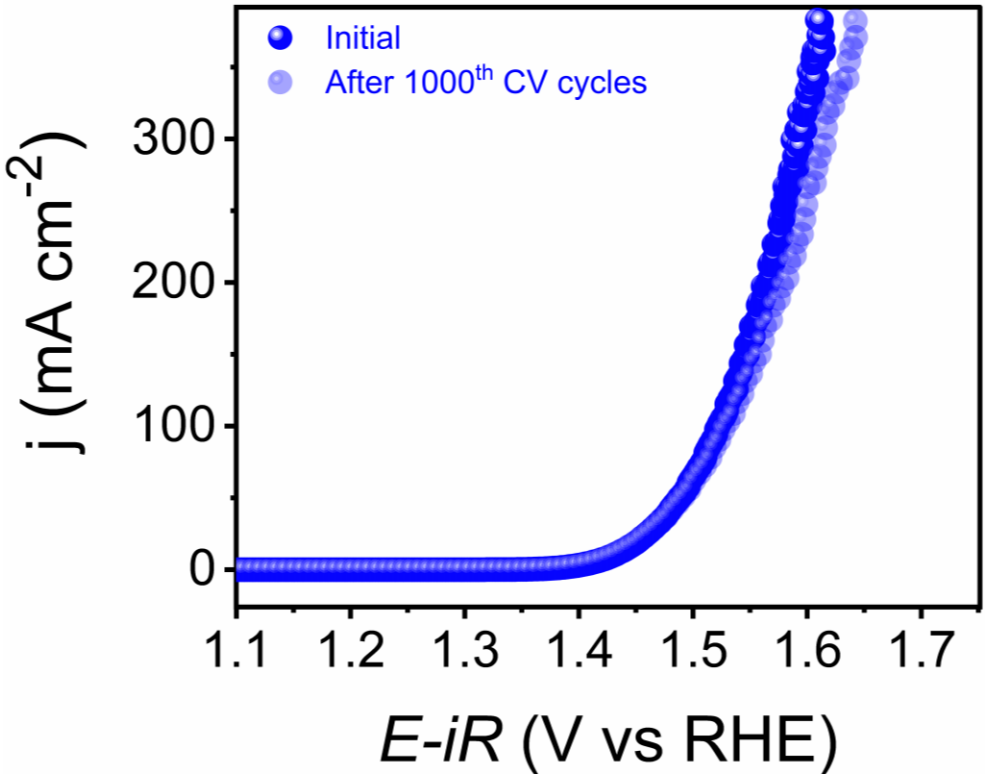

Figure S22: LSV curve of Ru_1/Ni-NPGC before and after CV cycles

S4.6. ECSA analysis

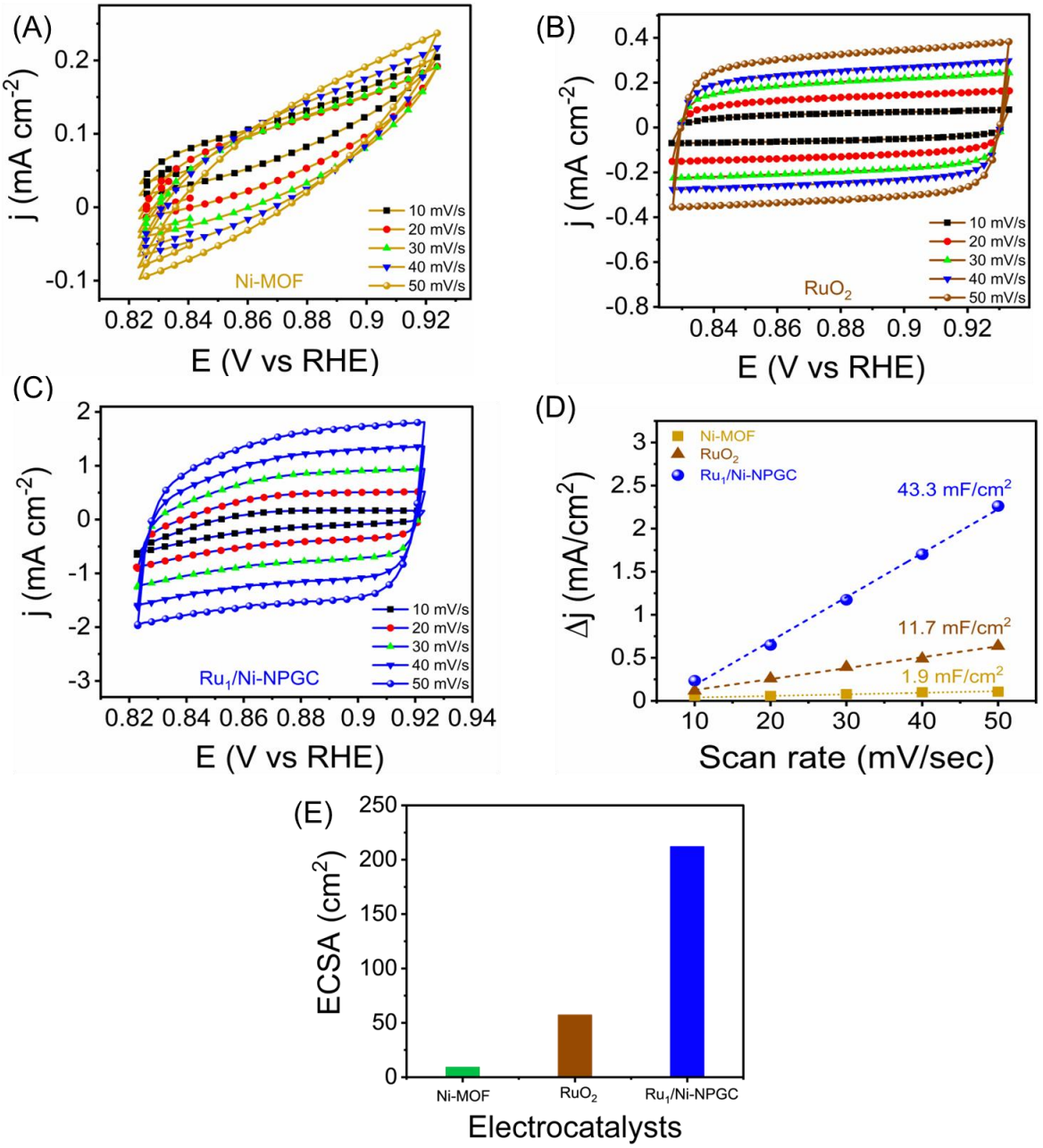

Figure S23: CVs were conducted in a non-Faradaic region of voltammogram at different scan rates (10,20,30,40,50 mV/sec) (A) Ni-MOF, (B) RuO_2, (C) Ru_1/Ni-NPGC, and (D) estimation of double-layer capacitance (C_{dl}), and (E) ECSA of electrocatalysts.

S4.7. Electrochemical impedance spectroscopy analysis

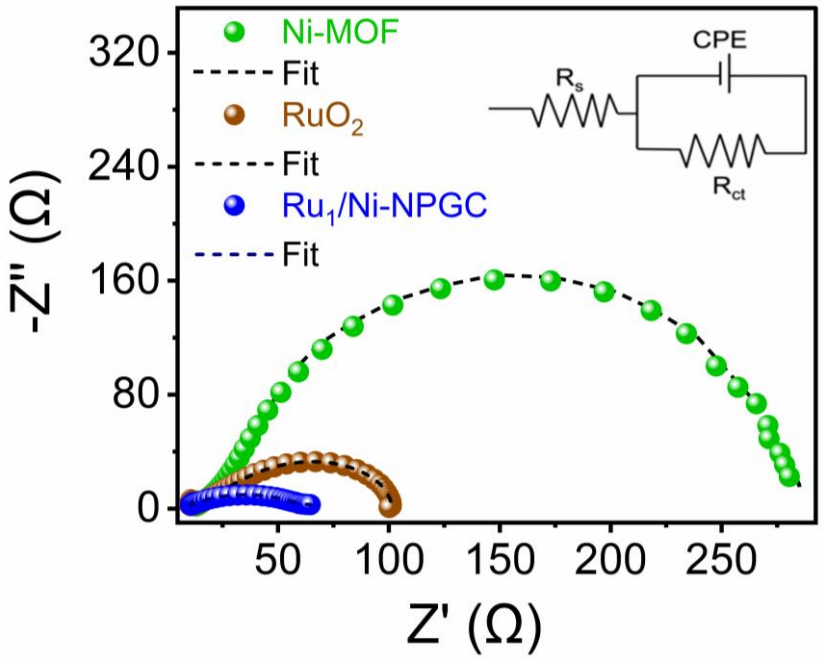

Figure S24: Nyquist plots of electrocatalysts recorded in 1 M KOH solution

S4.8. Post-electrolysis study

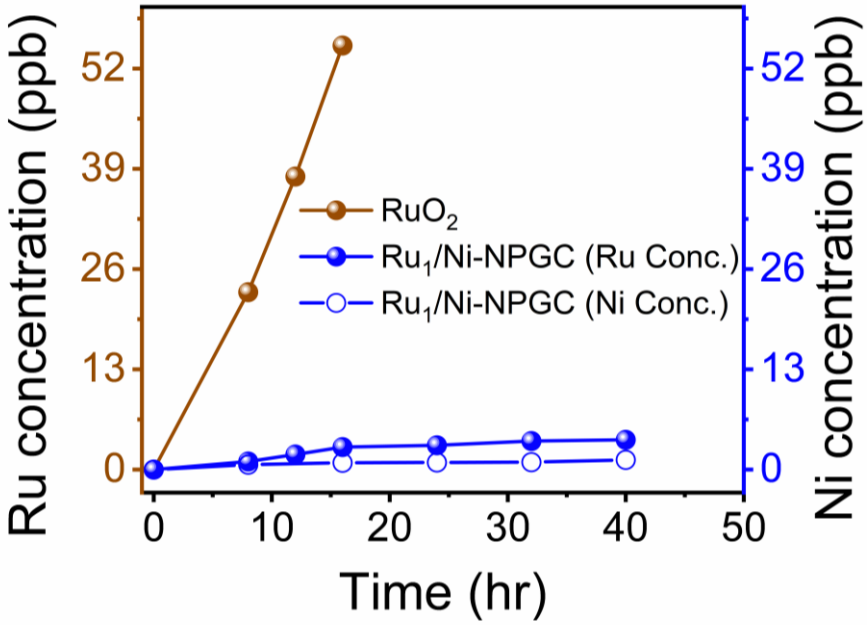

Figure S25: Dissolved Ru and Ni ion concentration in electrolyte for Ru_1/Ni-NPGC and RuO_2 determined using ICP-MS.

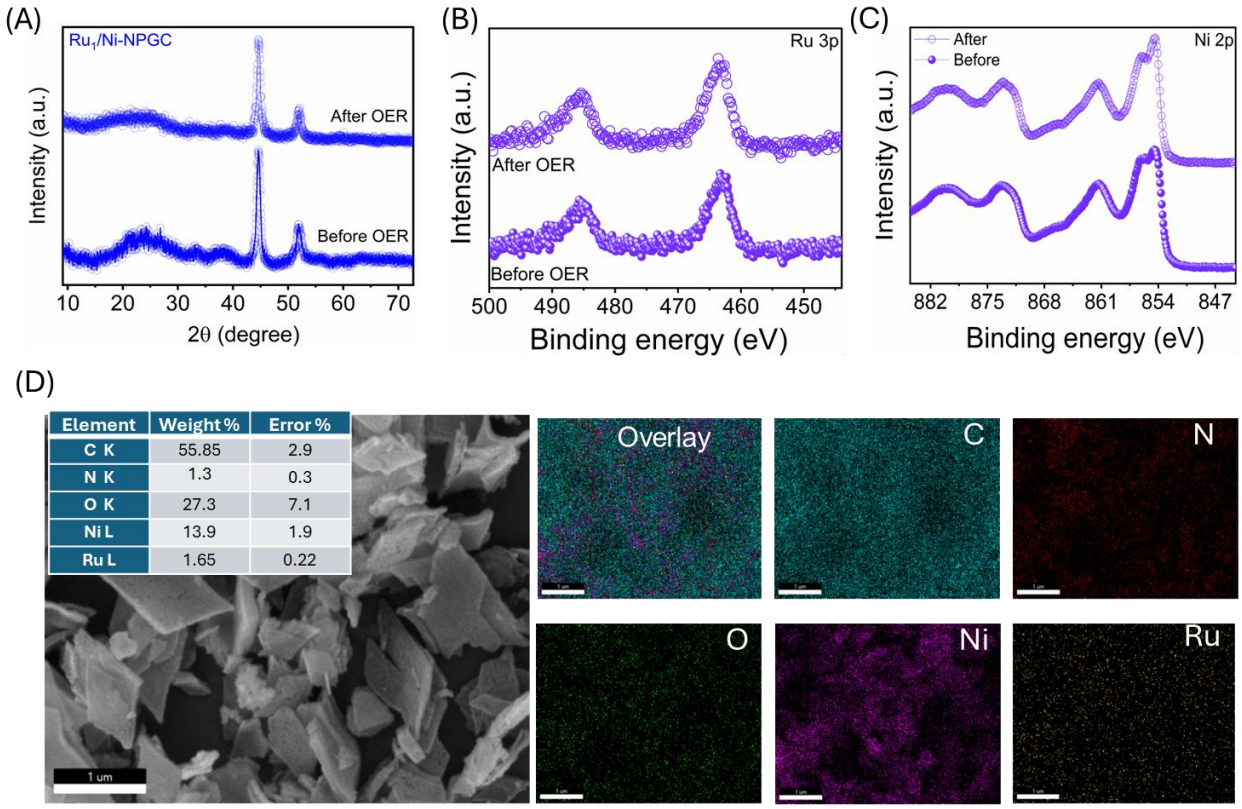

Figure S26: Post-electrocatalytic study of Ru_1/Ni-NPGC. (A) Before and after PXRD spectra, (B) Ru 3p XPS spectra, (C) Ni 2p XPS spectra, (D) FESEM-EDS mapping of Ru_1/Ni-NPGC after OER study.

S5: Additional data for HER

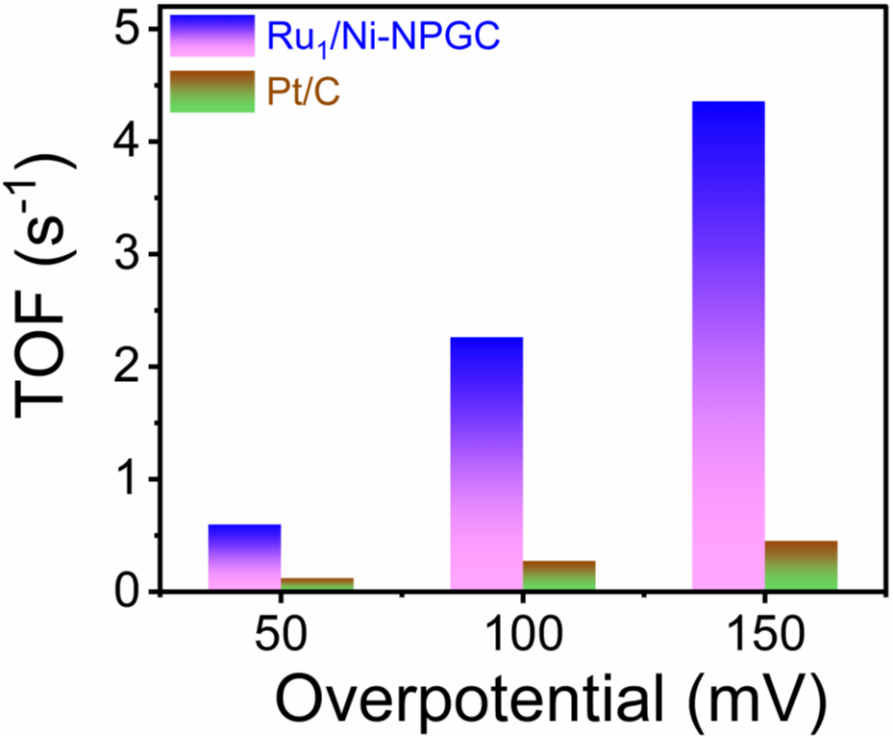

Figure S27: Turnover frequency (TOF) of the Ru_1/Ni-NPGC and Pt/C

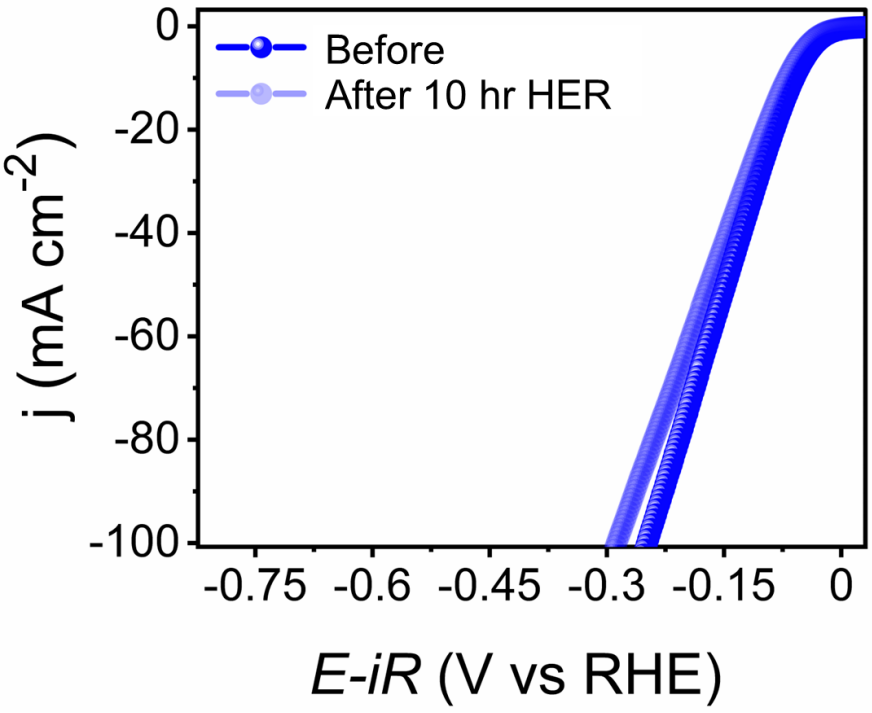

Figure S28: LSV curve of Ru_1/Ni-NPGC before and after 10 hr of HER operation.

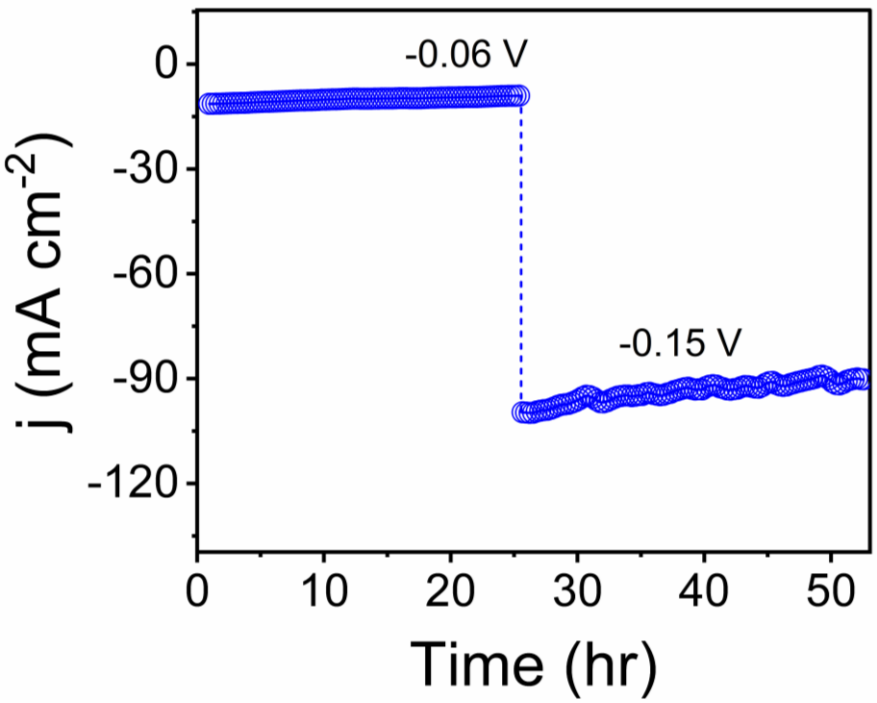

Figure S29: Chronoamperometric test of Ru_1/Ni-NPGC with current densities of 10 and 100 mA cm^{-2}

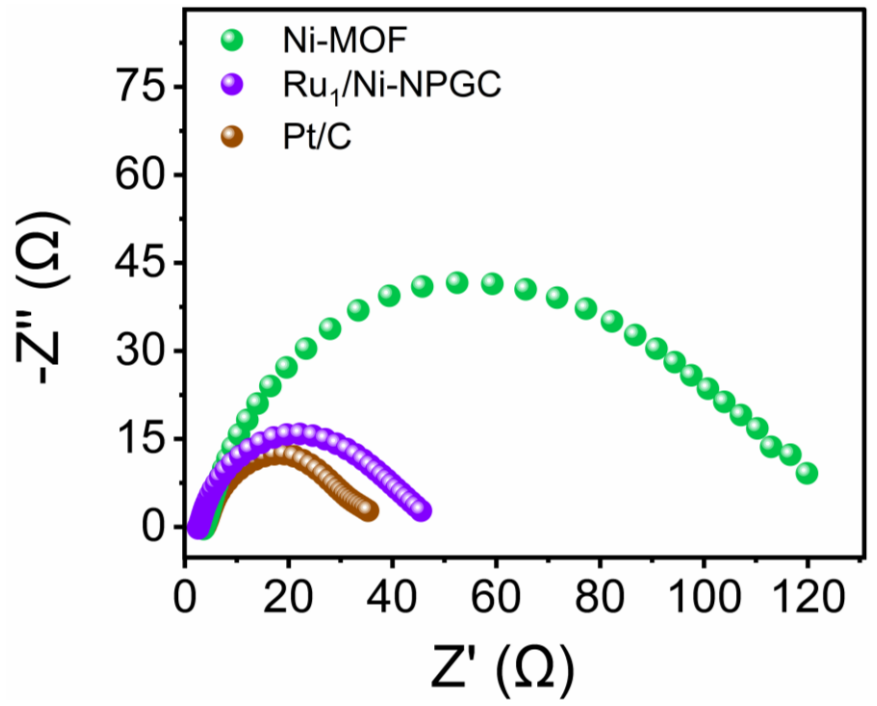

Figure S30: EIS spectra

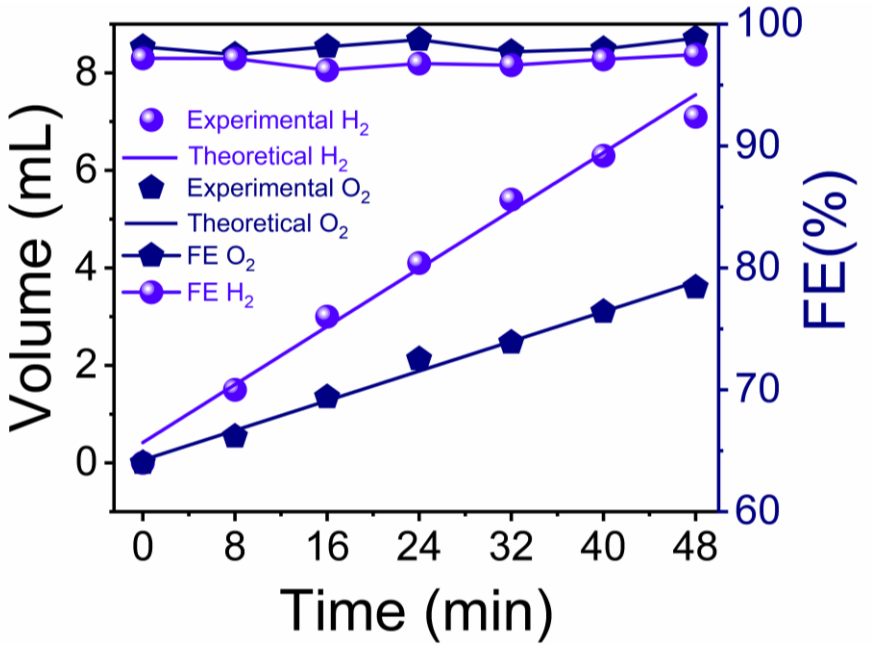

Figure S31: Experimental gas volumes of H_2 and O_2 during overall water splitting in 1M KOH, and the corresponding Faradaic efficiency of Ru_1/Ni-NPGC.

Table S1. EXAFS fitting parameters at the Ru K-edge for Ru-foil, RuO_2 and Ru_1/Ni-NPGC

Sample	Shell	CN	R (Å)	σ^2(Å^2)	R factor
Ru foil	Ru-Ru	12	2.61 ± 0.004	0.004± 0.0003	0.0026
RuO_2	Ru-O	6	1.97 ± 0.004	0.0034± 0.0004	0.0023
Ru_1/Ni-NPGC	Ru-N	4.1± 0.23	2.01 ± 0.006	0.0042± 0.0004	0.0027

CN: Coordination number, R is the bond length; σ^2 is the Debye-Waller factor, R-factor (%) indicates the goodness of the fit. S_0^2 was fixed to 0.92 which was determined from Ru foil fitting.

Table S2: OER Comparison table of Ru_1/Ni-NPGC with Pt/C and other reported catalysts in 1.0 M KOH

Electrocatalysts	Overpotential (mV)	Tafel slope (mV/dec)	References
Ru/Co_3O_{4-x}	280	86.9	[9]

Ru-NiCoP/NF	216	84.5	[10]
RuO_2/CeO_2	350 mV	74	[11]
CoO/Ru1.25% HPNs	308	58.89	[12]
Ru/CoFe-LDHs	198	39	[13]
CoRu-O/A@HNC-2	253	63.8	[14]
$Ir/Co(OH)_2$	200	70.2	[15]
Ru/Co-N-C-800℃	276	55.7	[16]
Ru_2Ni_2 SNs/C	310	75	[17]
$NiRu_{0.08}$-MOF (on Ni-Foam)	187	40	[18]
Ru, Ni-Co-P	251	102	[19]
RuIr@CoNC	223	45	[20]
Co_3O_4-Ru_1	249	66	[21]
RuCoN/$Ti_3C_2T_x$ MXene	238	68	[22]
$(Ru-Co)O_x$-350	265	60	[23]
NIBS1.2kV-100cyc	222	88	[24]
$Ni(OH)_2@Fe_xCo_1{-}xPi\|NiO$	133	45	[25]
Ru_1/Ni-NPGC	195	51.2	This work

Table S3: HER Comparison table of Ru_1/Ni-NPGC with Pt/C and other reported catalysts in 1.0 M KOH

Electrocatalysts	**Overpotential (mV)**	**Tafel slope (mV/dec)**	**References**
$C@Mo_2C/Co$	145	90.7	[26]
Ru-NPs/SAs@NTC	97	58	[27]
Co_3Mo_2-LDH	165	88	[28]
Ni_5P_4-Ru	54	52	[29]

Ru/NC	25	29	[30]
MoS_2/Ni_3S_2	81	78	[31]
RuP_2@NPC	52	69	[32]
R-TiO_2:Ru	150	97	[33]
$Ru/C_3N_4/C$	79	-	[34]
Rh_2P/XC-72	30	50	[35]
Sr2RuO4	61	51	[36]
Ru-MoO_2-Ni_4Mo	9	23	[37]
Ni_5P_4-Ru/CC	17	52	[29]
FTO/MoO_X/Pd	220	68	[38]
ECM@Ru	83	59	[39]
Ru_1/Ni-NPGC	54	39.1	This work

Table S4: Comparison of previously reported bifunctional electrocatalysts for overall water splitting under various pH conditions

Electrocatalyst	**Electrolyte**	**Cell voltage (V)**	**References**
Co-RuIr	0.1 M $HClO_4$	1.524	[40]
Ir/MoS_2 NFs	0.1 M $HClO_4$	1.55	[41]
h-PNRO/C	0.1 M $HClO_4$	1.524	[42]
RuO_2-WC NPs	0.5 M H_2SO_4	1.66	[43]
Ru_3Ni_3 NAs	0.5 M H_2SO_4	1.63	[44]
Ir WMWs	0.1 M $HClO_4$	1.62	[45]
Ru_3Ni_3 NAs	1M KOH	1.57	[44]
$RuIrO_x$	PBS	1.61	[46]

RhCo-ANAs	PBS	1.54	[47]
NiRu@MWCNTs	PBS	1.61	[48]
$RuIrO_x$	1M KOH	1.47	[46]
CoMoNiS-NF	1M KOH	1.54	[49]
RuCu NSs	1M KOH	1.49	[50]
Co/β-Mo_2C@N-CNTs	1M KOH	1.64	[51]
Ru-MoO_2-Ni_4Mo	1 M KOH + 0.5 M NaCl	1.5	[37]
Ru_1/Ni-NPGC	0.1M $HClO_4$ (pH 1)	1.5	This work
Ru_1/Ni-NPGC	PBS (pH 7.4)	1.55	This work
Ru_1/Ni-NPGC	1M KOH	1.48	This work

S5. References

1. B. Mishra, S. Biswal and B. P. Tripathi, *ACS Applied Nano Materials*, 2024, **7**, 5317-5328.
2. C. Feng, Z. Zhang, D. Wang, Y. Kong, J. Wei, R. Wang, P. Ma, H. Li, Z. Geng, M. Zuo, J. Bao, S. Zhou and J. Zeng, *Journal of the American Chemical Society*, 2022, **144**, 9271-9279.
3. S. Biswal, Divya, B. Mishra, D. Pohl, B. Rellinghaus, D. Ghosh and B. P. Tripathi, *Journal of Materials Chemistry A*, 2024, **12**, 2491-2500.
4. Y. Zhu, J. Wang, T. Koketsu, M. Kroschel, J.-M. Chen, S.-Y. Hsu, G. Henkelman, Z. Hu, P. Strasser and J. Ma, *Nature Communications*, 2022, **13**, 7754.
5. E. Cossar, M. S. E. Houache, Z. Zhang and E. A. Baranova, *Journal of Electroanalytical Chemistry*, 2020, **870**, 114246.
6. L. Cao, Q. Luo, J. Chen, L. Wang, Y. Lin, H. Wang, X. Liu, X. Shen, W. Zhang, W. Liu, Z. Qi, Z. Jiang, J. Yang and T. Yao, *Nature Communications*, 2019, **10**, 4849.
7. Z. Zhang, X.-G. Wang, X. Zhang, Z. Xie, Y.-N. Chen, L. Ma, Z. Peng and Z. Zhou, *Advanced Science*, 2018, **5**, 1700567.
8. T. Luo, J. Huang, Y. Hu, C. Yuan, J. Chen, L. Cao, K. Kajiyoshi, Y. Liu, Y. Zhao, Z. Li and Y. Feng, *Advanced Functional Materials*, 2023, **33**, 2213058.
9. C.-Z. Yuan, S. Wang, K. San Hui, K. Wang, J. Li, H. Gao, C. Zha, X. Zhang, D. A. Dinh, X.-L. Wu, Z. Tang, J. Wan, Z. Shao and K. N. Hui, *ACS Catalysis*, 2023, **13**, 2462-2471.
10. D. Chen, R. Lu, Z. Pu, J. Zhu, H.-W. Li, F. Liu, S. Hu, X. Luo, J. Wu, Y. Zhao and S. Mu, *Applied Catalysis B: Environmental*, 2020, **279**, 119396.
11. S. M. Galani, A. Mondal, D. N. Srivastava and A. B. Panda, *International Journal of Hydrogen Energy*, 2020, **45**, 18635-18644.
12. D. Guo, C. Chen, Y. Wang, Y. Wang and C. Zhang, *Journal of Materials Chemistry C*, 2023, **11**, 6336-6346.

13. P. Li, M. Wang, X. Duan, L. Zheng, X. Cheng, Y. Zhang, Y. Kuang, Y. Li, Q. Ma, Z. Feng, W. Liu and X. Sun, *Nature Communications*, 2019, **10**, 1711.
14. G. Li, K. Zheng, W. Li, Y. He and C. Xu, *ACS Applied Materials & Interfaces*, 2020, **12**, 51437-51447.
15. Y. Zhang, C. Wu, H. Jiang, Y. Lin, H. Liu, Q. He, S. Chen, T. Duan and L. Song, *Advanced materials*, 2018, **30**, 1707522.
16. C. Rong, X. Shen, Y. Wang, L. Thomsen, T. Zhao, Y. Li, X. Lu, R. Amal and C. Zhao, *Advanced materials*, 2022, **34**, 2110103.
17. J. Ding, Q. Shao, Y. Feng and X. Huang, *Nano Energy*, 2018, **47**, 1-7.
18. Y. Li, Y. Wu, T. Li, M. Lu, Y. Chen, Y. Cui, J. Gao and G. Qian, *Carbon Energy*, 2023, **5**, e265.
19. Y. Song, J. Cheng, J. Liu, Q. Ye, X. Gao, J. Lu and Y. Cheng, *Applied Catalysis B: Environmental*, 2021, **298**, 120488.
20. J. Xu, J. Li, Z. Lian, A. Araujo, Y. Li, B. Wei, Z. Yu, O. Bondarchuk, I. Amorim, V. Tileli, B. Li and L. Liu, *ACS Catalysis*, 2021, **11**, 3402-3413.
21. C. Zhao, Y. Tang, C. Yu, X. Tan, M. N. Banis, S. Li, G. Wan, H. Huang, L. Zhang, H. Yang, J. Li, X. Sun and J. Qiu, *Nano Today*, 2020, **34**, 100955.
22. L. Yan and B. Zhang, *Journal of Materials Chemistry A*, 2021, **9**, 20758-20765.
23. C. Wang, H. Shang, J. Li, Y. Wang, H. Xu, C. Wang, J. Guo and Y. Du, *Chemical Engineering Journal*, 2021, **420**, 129805.
24. W. S. Cheon, J. Bu, S. Jung, J.-Y. Yang, S. Choi, J. Kim, J. H. Baek, S. Park, M. K. Lee, S. E. Jun, S. H. Park, H. Park, S. A. Lee, S. H. Cho, M. Shokouhimehr, M. Senna and H. W. Jang, *Chemical Engineering Journal*, 2024, **489**, 151004.
25. S. Marimuthu, A. Shankar and G. Maduraiveeran, *Chemical Communications*, 2024, **60**, 1345-1348.
26. L. Xia, X. Zhang, H. Song, Y. Zheng, X. Li, B. Gao, K. Huo and P. K. Chu, *International Journal of Hydrogen Energy*, 2020, **45**, 22629-22637.
27. B. Yan, D. Liu, X. Feng, M. Shao and Y. Zhang, *Advanced Functional Materials*, 2020, **30**, 2003007.
28. S. M. N. Jeghan, J. Kim and G. Lee, *Applied Surface Science*, 2021, **546**, 149072.
29. Q. He, D. Tian, H. Jiang, D. Cao, S. Wei, D. Liu, P. Song, Y. Lin and L. Song, *Advanced materials*, 2020, **32**, 1906972.
30. Y. Zhu, K. Fan, C.-S. Hsu, G. Chen, C. Chen, T. Liu, Z. Lin, S. She, L. Li, H. Zhou, Y. Zhu, H. M. Chen and H. Huang, *Advanced materials*, 2023, **35**, 2301133.
31. M. Wang, M. Zhang, W. Song, W. Zhong, X. Wang, J. Wang, T. Sun and Y. Tang, *Chemical Communications*, 2021, **57**, 785-788.
32. Z. Pu, I. S. Amiinu, Z. Kou, W. Li and S. Mu, *Angewandte Chemie International Edition*, 2017, **56**, 11559-11564.
33. S. Nong, W. Dong, J. Yin, B. Dong, Y. Lu, X. Yuan, X. Wang, K. Bu, M. Chen, S. Jiang, L.-M. Liu, M. Sui and F. Huang, *Journal of the American Chemical Society*, 2018, **140**, 5719-5727.
34. Y. Zheng, Y. Jiao, Y. Zhu, L. H. Li, Y. Han, Y. Chen, M. Jaroniec and S.-Z. Qiao, *Journal of the American Chemical Society*, 2016, **138**, 16174-16181.
35. F. Yang, Y. Zhao, Y. Du, Y. Chen, G. Cheng, S. Chen and W. Luo, *Advanced Energy Materials*, 2018, **8**, 1703489.
36. Y. Zhu, H. A. Tahini, Z. Hu, J. Dai, Y. Chen, H. Sun, W. Zhou, M. Liu, S. C. Smith, H. Wang and Z. Shao, *Nature Communications*, 2019, **10**, 149.
37. S. E. Jun, S.-W. Myeong, B.-G. Cho, J. Kim, S. J. Park, C. Kim, T. H. Lee, S. Lee, J. Y. Kim, M. S. Kwon, J. H. Kang, K. C. Kwon, S. M. Choi, H. W. Jang and S. H. Park, *Applied Catalysis B: Environment and Energy*, 2024, **358**, 124364.
38. U. K. Ghorui, B. Show, D. Roy, A. Basak, B. Adhikary and A. Mondal, *ACS Applied Materials & Interfaces*, 2024, **16**, 3460-3475.
39. H. Zhang, W. Zhou, X. F. Lu, T. Chen and X. W. Lou, *Advanced Energy Materials*, 2020, **10**, 2000882.
40. J. Shan, T. Ling, K. Davey, Y. Zheng and S.-Z. Qiao, *Advanced materials*, 2019, **31**, 1900510.

41. C. Wang, L. Yu, F. Yang and L. Feng, *Journal of Energy Chemistry*, 2023, **87**, 144-152.
42. A. Oh, H. Y. Kim, H. Baik, B. Kim, N. K. Chaudhari, S. H. Joo and K. Lee, *Advanced materials*, 2019, **31**, 1805546.
43. S.-C. Sun, H. Jiang, Z.-Y. Chen, Q. Chen, M.-Y. Ma, L. Zhen, B. Song and C.-Y. Xu, *Angewandte Chemie International Edition*, 2022, **61**, e202202519.
44. J. Yang, Q. Shao, B. Huang, M. Sun and X. Huang, *iScience*, 2019, **11**, 492-504.
45. L. Fu, F. Yang, G. Cheng and W. Luo, *Nanoscale*, 2018, **10**, 1892-1897.
46. Z. Zhuang, Y. Wang, C.-Q. Xu, S. Liu, C. Chen, Q. Peng, Z. Zhuang, H. Xiao, Y. Pan, S. Lu, R. Yu, W.-C. Cheong, X. Cao, K. Wu, K. Sun, Y. Wang, D. Wang, J. Li and Y. Li, *Nature Communications*, 2019, **10**, 4875.
47. Y. Zhao, J. Bai, X.-R. Wu, P. Chen, P.-J. Jin, H.-C. Yao and Y. Chen, *Journal of Materials Chemistry A*, 2019, **7**, 16437-16446.
48. Z. Peng, J. Liu, B. Hu, Y. Yang, Y. Guo, B. Li, L. Li, Z. Zhang, B. Cui, L. He and M. Du, *ACS Applied Materials & Interfaces*, 2020, **12**, 13842-13851.
49. Y. Yang, H. Yao, Z. Yu, S. M. Islam, H. He, M. Yuan, Y. Yue, K. Xu, W. Hao, G. Sun, H. Li, S. Ma, P. Zapol and M. G. Kanatzidis, *Journal of the American Chemical Society*, 2019, **141**, 10417-10430.
50. Q. Yao, B. Huang, N. Zhang, M. Sun, Q. Shao and X. Huang, *Angewandte Chemie International Edition*, 2019, **58**, 13983-13988.
51. T. Ouyang, Y.-Q. Ye, C.-Y. Wu, K. Xiao and Z.-Q. Liu, *Angewandte Chemie International Edition*, 2019, **58**, 4923-4928.